(Received 15 June 2024, Accepted 4 August 2024, Scheduled 17 August 2024)

New Non-Singular Fast Terminal Sliding Mode Control of Permanent Magnet Synchronous Motor Based on Super-Twisting Sliding Mode Observer

Jiaoyang Wang[1, *], Renjun Zhou[1], and Junqin Liu[2]

[1] College of Electrical and Information Engineering
Changsha University of Science & Technology, Changsha 410114, Hunan, China
[2] College of Electrical and Information Engineering, Hunan University of Technology, Zhuzhou 412007, China

ABSTRACT: To address the problem of traditional speed loop controllers being unable to achieve rapid system convergence in the face of complex external operating conditions, this paper designs a new nonsingular fast terminal sliding mode control algorithm (NNFTSMC) for PMSM with a super twisting sliding mode perturbation observer (STSMO). Firstly, the mathematical models of PMSM for ideal case and parametric composite uptake are established. Secondly, a new non-singular fast terminal sliding mode control surface (NNFTSM) is proposed to design the PMSM speed-loop controller, which is also paired with the STSMO to observe the total system perturbation in real time and compensate the perturbation to the speed-loop NNFTSMC controller to form a new composite controller of NNFTSMC+STSMO. Finally, the proposed composite control algorithm of NNFTSMC+STSMO is verified to be effective in improving the control of the PMSM drive system during the parameters and load mutation by comparing simulation and RT-Lab semi-physical experiments.

1. INTRODUCTION

PMSM becomes computer numerical control (CNC) machine tools, instrumentation, aerospace, and other strict requirements for the system control performance of the field for research hot spots because of its simple structure, control accuracy, and other advantages [1]. Meanwhile, proportional-integral (PI) controller is widely used in PMSM drive system because of its simple structure [2]. However, PI controller often leads to substandard system control accuracy because of its linearization. Therefore, a wide range of scholars have proposed a variety of improved algorithms based on the PI control mechanism in recent years, including Model Predictive Control (MPC) [3], Sliding Mode Control (SMC) [4], and Robust Control (RC) [5].

The SMC algorithm has been developed in the field of nonlinear control, such as PMSM system, due to its low model accuracy requirement, insensitivity to nonlinear perturbation, and simplicity of physical implementation [6]. Compared with traditional PI controller, the traditional SMC control algorithm based on Sliding Mode Disturbance Observer (SMO) can suppress the effects of parameters uptake and load perturbation to a certain extent. When SMO estimates the total system disturbance and feeds it back to the SMC controller, the convergence performance of the linear integral sliding mode surface in traditional SMC is poor. In high-precision and high-quality applications, the system error cannot quickly converge to 0 in a finite time [7]. In complex operating environments, PI controller and SMO-based conventional SMC controller are difficult to suppress the sudden increase of jitter in a PMSM drive system, which affects the efficiency and safe operation of PMSM system [8].

Ref. [9] proposes the Model Free Sliding Mode Control (MFSMC) algorithm based on the traditional SMC combined with the model-free theory, and the simulated and experimental results prove that it can improve the response speed of the PMSM drive system compared with the traditional SMC. To improve the large jitter problem of the conventional integral sliding mode, [10] proposes a fast super-twisting non-singular fast terminal sliding mode controller with a higher-order Kalman algorithm instead of sensors to estimate the speed and rotor position. Ref. [11] proposes a new type of fast integrating terminal sliding mode surface and uses it to design a higher-order sliding mode controller and observer. The simulations and experiments demonstrate that the higher-order terminal sliding mode can effectively solve the large jittering defect inherent in the traditional integral SMC. Ref. [12] combines the second-order super-twisting algorithm and fast terminal switching function to design a super-twisting fast terminal sliding mode controller. Compared to [11], its composite controller has a simpler structure with fewer parameters which can further improve the anti-interference ability and tracking performance of system. Ref. [13] suggests that the traditional second-order super-twisting algorithm will cause the system to converge too slowly due to the absence of the linear term, and the exponent of its state vector is always 1/2, which does not minimize the convergence of the system state. Therefore, [14] proposes a third-order super-twisting algorithm, which adds a fast term to

* Corresponding author: Jiaoyang Wang (wjyzhiaixuexi@163.com).

the second-order super-twisting algorithm, and it can perfectly solve the problem that the system converges too slowly.

Aiming at the above problems, in order to ensure the fast convergence of the system while weakening the system jitter considering the complex working conditions such as PMSM parameter uptake and external perturbations, this paper designs a new non-singular fast terminal sliding mode composite control method (NNFTSMC) based on the Super-twisting Sliding Mode Observer (STESMO).

The method designs a speed-loop controller for PMSM by proposing a new non-singular fast terminal sliding mode surface. It also proposes the super-twisting control law to design STESMO, and STESMO can observe the total system perturbation in real time and compensate the perturbation to NNFTSMC, which can effectively improve the anti-interference ability and robustness of the PMSM speed control system. Finally, simulation and RT-Lab semi-physical experimental results verify the effectiveness and superiority of the proposed algorithm.

2. METHODS MATHEMATICAL MODEL OF PMSM

2.1. Mathematical Model of PMSM under Ideal Operating Condition

Neglecting all losses [15], the d-q axis stator voltage equation with the PMSM in ideal operation is expressed as:

$$\begin{cases} u_d = R_s i_d + \frac{d}{dt}\psi_d - \omega_e \psi_q \\ u_q = R_s i_q + \frac{d}{dt}\psi_q + \omega_e \psi_d \end{cases} \tag{1}$$

In Eq. (1), the equation for the stator magnetic chain is expressed as:

$$\begin{cases} \psi_d = L_d i_d + \psi_f \\ \psi_q = L_q i_q \end{cases} \tag{2}$$

From Eq. (1) and Eq. (2), the following expression can be expressed as:

$$\begin{cases} u_d = R_s i_d + L_d \frac{di_d}{dt} - \omega_e L_q i_q \\ u_q = R_s i_q + L_q \frac{di_q}{dt} + \omega_e \left(L_d i_d + \psi_f\right) \end{cases} \tag{3}$$

where R_s is the stator resistance; ψ_f is the chain of permanent magnet; ω_e is the electrical angular velocity; u_d is the stator voltage component in the d-axis; u_q is the stator voltage component in the q-axis; i_d is the stator current component in the d-axis; i_q is the stator current component in the q-axis; L_d is the stator inductance in d-axis; L_q is the stator inductance in q-axis.

The d-q axis electromagnetic torque equation for the PMSM is expressed as [16]:

$$T_e = \frac{3}{2} n_p \left[\psi_f + \left(L_d - L_q\right) i_d\right] i_q = \frac{3}{2} n_p \psi_e i_q \tag{4}$$

where T_e is the electromagnetic torque output; n_p is the pole number; $\psi_e = \psi_f + (L_d - L_q) i_d$, ψ_e is the effective flux.

The mechanical equation of motion for PMSM is expressed as [17]:

$$\frac{J}{n_p} \cdot \frac{d\omega_e}{dt} = T_e - T_L - B\omega_m \tag{5}$$

where B is the damping coefficient; J is the moment of inertia; ω_m is the mechanical angular speed; T_L is the load torque.

Substituting Eq. (4) into Eq. (5), the rotational speed equation of state is expressed as [18]:

$$\frac{d\omega_e}{dt} = \frac{3n_p^2}{2J} \psi_e i_q - \frac{B}{J} \omega_e - \frac{n_p}{J} T_L \tag{6}$$

2.2. Mathematical Model of PMSM under Varying Condition of Motor Parameters

In the actual operating environment, the PMSM electromagnetic parameter variation equation can be expressed as:

$$\begin{cases} \tilde{R}_s = R_s + \Delta R_s \\ \tilde{L}_d = L_d + \Delta L_d \\ \tilde{L}_q = L_q + \Delta L_q \\ \tilde{\psi}_f = \psi_f + \Delta \psi_f \end{cases} \tag{7}$$

where $\tilde{R}_s$, $\tilde{L}_d$, $\tilde{L}_q$, $\tilde{\psi}_f$ are the actual values of electromagnetic parameters for PMSM under parameters ingestion and external time-varying disturbance; ΔR_s, ΔL_d, ΔL_q, $\Delta \psi_f$ are the corresponding values of the uptake.

In the actual operating environment, the equations for the mechanical parameters of the PMSM and the variation of the external load are expressed as:

$$\begin{cases} \tilde{B} = B + \Delta B \\ \tilde{T}_L = T_L + \Delta T_L \\ \tilde{J} = J + \Delta J \end{cases} \tag{8}$$

where $\tilde{B}$ and $\tilde{J}$ are the actual values of mechanical parameters for PMSM under parameters ingestion and external time-varying disturbance; $\tilde{T}_L$ is the actual value of load for PMSM; ΔB, ΔJ, ΔT_L are the corresponding values of the uptake.

From Eq. (7) and Eq. (8), Eq. (1) can be rewritten as:

$$\begin{cases} u_d = R_s i_d + \frac{d\psi_d}{dt} - \omega_e \psi_q + \Delta u_d \\ u_q = R_s i_q + \frac{d\psi_q}{dt} + \omega_e \psi_d + \Delta u_q \end{cases} \tag{9}$$

where Δu_d, Δu_q are the perturbation of the d-q axis voltage, and they can be expressed as:

$$\begin{cases} \Delta u_d = \Delta R_s i_d + \frac{d\Delta\psi_d}{dt} - \omega_e \Delta \psi_q \\ \Delta u_q = \Delta R_s i_q + \frac{d\Delta\psi_q}{dt} + \omega_e \Delta \psi_d \end{cases} \tag{10}$$

When the parameters of the PMSM are subjected to compound ingress, the electromagnetic torque equation of the PMSM is transformed by Eq. (4) as:

$$T_e = \frac{3}{2} n_p \left[\tilde{\psi}_f + (\tilde{L}_d - \tilde{L}_q) i_d\right] i_q$$

$$= \frac{3}{2} n_p \left[\psi_f + (L_d - L_q) i_d\right] i_q + \Delta T_e$$
$$= \frac{3}{2} n_p \psi_{ext} i_q + \Delta T_e \quad (11)$$

where ΔT_e is the uptake of the electromagnetic torque, and it can be expressed as:

$$\Delta T_e = \frac{3}{2} n_p \left[\Delta\psi_f + (\Delta L_d - \Delta L_q) i_d\right] i_q \quad (12)$$

When the parameters of the PMSM are subjected to compound ingress, Eq. (6) can be rewritten as:

$$\frac{d\omega_e}{dt} = \frac{n_p}{\tilde{J}} \left(T_e - \tilde{T}_L - \tilde{B}\omega_m\right) + \Delta P_n \quad (13)$$

where ΔP_n is the unknown perturbation caused by the uptake of the B and J.

When the parameters of the PMSM are subjected to compound ingress, from Eqs. (11) and (13), Eq. (14) can be obtained as [19]:

$$\begin{aligned}\frac{d\omega_e}{dt} &= \frac{3n_p^2}{2\tilde{J}} \psi_{ext} i_q - \frac{\tilde{B}}{\tilde{J}} \omega_e - \frac{n_p}{\tilde{J}} \tilde{T}_L \\ &= \frac{3n_p^2}{2J} \psi_{ext} i_q - \frac{B}{J} \omega_e \\ &\quad + \left[\frac{n_p}{J} (\Delta T_e - T_L + \Delta T_L) + \Delta P_n + \Delta D\right] \\ &= \lambda_1 i_q + \lambda_2 \omega_e + F \end{aligned} \quad (14)$$

where $\lambda_1 = 3n_p^2\psi_{ext}/2J$; $\lambda_2 = -B/J$; F is the total bounded perturbation.

3. DESIGN OF THE NNFTSMC BASED ON STESMO

3.1. Design of Speedloop Controller of NNFTSMC for PMSM

From Eq. (14), the control law for designing the speed controller can be expressed as:

$$i_q^* = \frac{\dot{\omega}_e^* - \lambda_2\omega_e - F + u_1}{\lambda_1} \quad (15)$$

where ω_e^* is the given speed; u_1 is the output of NNFTSMC; i_q^* is the given q-axis current.

From Eq. (15) and Eq. (14), $\dot{\omega}_e^* - \dot{\omega}_e + u_1 = 0$, and the state error of the controller is $e = \omega_e^* - \omega_e$. Eq. (16) can be expressed as:

$$\begin{cases} \dot{e}_1 = e_2 = \omega_e^* - \omega_e \\ \dot{e}_2 = \dot{e} = \dot{\omega}_e^* - \dot{\omega}_e \end{cases} \quad (16)$$

Based on the traditional NFTSM surface, the new NFTSM surface (NNFTSM) is designed as [20]:

$$s = e_1 + a_1 e_1^{l_1} + a_2 e_2^{l_2} + e_2 \quad (17)$$

where $a_1 > 0$; $a_2 > 0$; $l_1 = p/q$, $l_2 = g/h$, $g > 0$, $h > 0$, $p > 0$, $q > 0$; $1 < l_1 < 2$, $l_2 > l_1$.

Taking the derivative of Eq. (17):

$$\begin{aligned}\dot{s} &= \dot{e}_1 + a_1 l_1 e_1^{l_1-1} e_2 + a_2 l_2 e_2^{l_2-1} \dot{e}_2 \\ &= e_2 + a_1 l_1 e_1^{l_1-1} e_2 + \left(a_2 l_2 e_2^{l_2-1} + 1\right) \dot{e}_2 \end{aligned} \quad (18)$$

The design index convergence law is expressed as [21]:

$$\dot{s} = -\eta_1 \mathrm{sgn}(s) - \eta_2 s \quad (19)$$

where $\eta_1 > 0$; $\eta_2 > 0$.

Let the s in Eq. (17) be equal to 0:

$$e_2 = -e_1 - a_1 e_1^{l_2} - a_2 e_2^{l_1} \quad (20)$$

Let the s and $\dot{s}$ in Eq. (17) be equal to 0, and u_1 is expressed as:

$$u_1 = \begin{bmatrix} \left(1 + a_2 l_2 e_2^{l_2-1}\right)^{-1} \cdot \left(e_2 + a_1 l_1 e_2 e_1^{l_1-1}\right) \\ +\eta_1 \mathrm{sgn}(s) + \eta_2 s \end{bmatrix} \quad (21)$$

From Eqs. (21) and (15), Eq. (22) can be obtained as i_q^* for:

$$i_q^* = \frac{1}{\lambda_1} \begin{bmatrix} \left(1 + a_2 l_2 e_2^{l_2-1}\right)^{-1} \cdot \left(e_2 + a_1 l_1 e_2 e_1^{l_1-1}\right) \\ +\dot{\omega}_e^* - \lambda_2\omega_e + \eta_1 \mathrm{sgn}(s) + \eta_2 s - F \end{bmatrix} \quad (22)$$

Theorem 1: According to Eqs. (17), (19), and (21), while $\eta_1 \geq \left\|\tilde{F}\right\| + \rho$, the designed NNFTSMC is stabilized, and the convergence time T_s can be expressed as:

$$T_s \leq \frac{\ln\left(1 + \exp^{\varepsilon\tau t} V_{(0)}^{\tau}\right)}{\varepsilon\tau} \quad (23)$$

Proof: To illustrate the stability of NNFTSMC, the Lyapunov function V_1 is chosen as:

$$V_1 = \frac{1}{2} s^2 \quad (24)$$

Taking the derivative of V_1:

$$\begin{aligned}\dot{V} &= s\left[e_2 + a_1 l_1 e_1^{l_1-1} e_2 + \left(a_2 l_2 e_2^{l_2-1} + 1\right) \dot{e}_2\right] \\ &= s \begin{bmatrix} e_2 + a_1 l_1 e_1^{l_1-1} e_2 + \left(a_2 l_2 e_2^{l_2-1} + 1\right) \\ \cdot \begin{pmatrix} -\left(1 + a_2 l_2 e_2^{l_2-1}\right)^{-1} \cdot \left(e_2 + a_1 l_1 e_2 e_1^{l_1-1}\right) \\ -\eta_1 \mathrm{sgn}(s) - \eta_2 s \end{pmatrix} \end{bmatrix} \\ &= s \begin{bmatrix} e_2 + a_1 l_1 e_1^{l_1-1} e_2 - \left(e_2 + a_1 l_1 e_2 e_1^{l_1-1}\right) \\ + \left(a_2 l_2 e_2^{l_2-1} + 1\right) \left(\hat{F} - F - \eta_2 s - \eta_1 \mathrm{sgn}(s)\right) \end{bmatrix} \\ &= s\left[\left(a_2 l_2 e_2^{l_2-1} + 1\right) \left(\|\hat{F}\| - \eta_2 s - \eta_1 \mathrm{sgn}(s)\right)\right] \\ &\leq \left(a_2 l_2 e_2^{l_2-1} + 1\right) \left(\left(\|\hat{F}\| - \eta_1\right) \|s\| - \eta_2 \|s\|^2\right) \end{aligned} \quad (25)$$

$a_2 l_2 e_2^{l_2-1}+1>0$, from Eq. (25), while $\eta_1 \geq \left\|\tilde{F}\right\|+\rho\,(\rho>0)$, $\dot{V}\leq 0$, the designed of NNFTSMC is stable [22]. To further demonstrate the convergence time of the system T_s, the Lyapunov function V is chosen to be

$$V=\frac{1}{2}e_1^2 \tag{26}$$

Taking the derivative of Eq. (26)

$$\begin{aligned}\dot{V} &= e_1\dot{e}_1 = e_1 e_2 = e_1\left(-e_1-a_1 e_1^{l_1}-a_2 e_2^{l_2}\right)\\ &= -e_1^2-a_1 e_1^{l_1+1}-a_2 e_1 e_2^{l_2}\\ &= -2V-2a_1 V^{(l_1+1)/2}-a_2 e_2^{l_2-1}\dot{V}\end{aligned} \tag{27}$$

Eq. (27) is rewritten as:

$$\left(1+a_2 e_2^{l_2-1}\right)\dot{V}=-2V-2a_1 V^{(l_1+1)/2} \tag{28}$$

From Eq. (28), $\dot{V}$ follows as:

$$\dot{V}=-2\,\frac{V+a_1 V^{(l_1+1)/2}}{1+a_2 e_2^{l_2-1}} \tag{29}$$

Since $1<l_2=g/h<2$, $g>0$, and $h>0$, the equation as in Eq. (30) can be obtained as:

$$l_2-1=\frac{g-h}{h}=\frac{2k}{h},\quad (k=1,2\cdots) \tag{30}$$

Then $a_2 e_2^{l_2-1}=a_2 e_2^{2k/h}\geq 0$, Eq. (31) can be obtained as:

$$\frac{dV}{dt}\leq -\frac{V+a_1 V^{(l_1+1)/2}}{1+a_2 e_2^{2k/h}}=-\varepsilon\left(V+a_1 V^{(l_1+1)/2}\right) \tag{31}$$

where $\mu=(1+a_2 e_2^{2k/h})^{-1}>0$. Multiplying both sides by $V^{2/(l_1+1)}(l_1+3)/(l_1+1)$ at the same time, Eq. (32) can be obtained as:

$$\frac{l_1+3}{l_1+1}V^{\frac{2}{l_1+1}}\frac{dV}{dt}\leq -\mu\,\frac{l_1+3}{l_1+1}V^{\frac{2}{l_1+1}}\left(V+a_1 V^{\frac{l_1+1}{2}}\right) \tag{32}$$

Rewriting Eq. (32) as follows:

$$\frac{dV^\tau}{dt}\leq -\mu\tau\left(V^\tau+a_1\right)=-\mu\tau V^\tau-\mu\tau a_1 \tag{33}$$

where $(l_1+3)/(l_1+1)=\tau>0$.

From Eq. (33):

$$\frac{dV^\tau}{dt}+\mu\tau V^\tau\leq -\mu\tau a_1 \tag{34}$$

Multiplying both sides by $\exp^{\mu\tau t}$ at the same time:

$$\exp^{\mu\tau t}\left(\frac{dV^\tau}{dt}+\mu\tau V^\tau\right)\leq -\mu\tau a_1\exp^{\mu\tau t} \tag{35}$$

Rewriting Eq. (35) as follows:

$$\frac{d\left(\exp^{\mu\tau t}V^\tau\right)}{dt}\leq -\mu\tau a_1\exp^{\mu\tau t} \tag{36}$$

From Eq. (36), T_s is designed as $\int_0^{T_s}dV=V_{(T_s)}-V_{(0)}$, and $V_{(T_s)}=0$.

Integrating both sides of Eq. (36) simultaneously:

$$-\exp^{\mu\tau t}V_{(0)}^\tau\leq -\frac{\mu\tau a_1}{\varepsilon\tau}\left(\exp^{\mu\tau T_s}-1\right)=-a_1\left(\exp^{\mu\tau T_s}-1\right) \tag{37}$$

Eq. (37) can be rewritten as:

$$\exp^{\mu\tau T_s}\leq 1+\frac{\exp^{\mu\tau t}V_{(0)}^\tau}{a_1} \tag{38}$$

Taking exp as the base logarithm for Eq. (38):

$$\mu\tau T_s\leq \ln\left(1+\frac{\exp^{\mu\tau t}V_{(0)}^\tau}{a_1}\right) \tag{39}$$

From Eq. (39), the final expression of T_s is rewritten as:

$$T_s\leq \frac{\ln\left(1+\frac{\exp^{\mu\tau t}V_{(0)}^\tau}{a_1}\right)}{\mu\tau} \tag{40}$$

3.2. Design of STSMO for NNFTSMC

Defining $x=\hat{\omega}_e-\omega_e$, Eq. (41) can be rewritten as:

$$\begin{cases}\frac{d\hat{\omega}_e}{dt}=\lambda_1 i_q+\lambda_2\hat{\omega}_e+\hat{F}+u_{stsmo}\\ \frac{d\tilde{F}}{dt}=G\cdot u_{stsmo}\end{cases} \tag{41}$$

where $\hat{\omega}_e$ and $\hat{F}$ are the observed values of ω_e and F, respectively; u_{stsmo} is the control law of the STSMO.

From Eq. (14) and Eq. (41), Eq. (42) is rewritten as:

$$\begin{cases}\dot{x}=\lambda_2 x+\tilde{F}+u_{stsmo}\\ \frac{d\tilde{F}}{dt}=G\cdot u_{stsmo}-\ell(t)\end{cases} \tag{42}$$

where $\tilde{F}=\hat{F}-F$; $\ell(t)=dF/dt$.

Taking $s_1=x=\hat{\omega}_e-\omega_e$ to be the sliding mold surface, the design of the ST control law is [23]:

$$\begin{cases}\dot{s}_1=-r_1\left|s_1\right|^{\frac{1}{2}}\mathrm{sgn}\left(s_1\right)+g+F\\ \dot{g}=-r_2\mathrm{sgn}\left(s_1\right)\end{cases} \tag{43}$$

From Eq. (42)~Eq. (44), u_{stsmo} can be expressed as:

$$u_{stsmo}=\begin{bmatrix}-\lambda_2 x-r_1\left|s_1\right|^{\frac{1}{2}}\mathrm{sgn}\left(s_1\right)\\ -\int_0^t r_2\mathrm{sgn}\left(s_1\right)dt\end{bmatrix} \tag{44}$$

Theorem 2: According to Eq. (41)∼Eq. (44), the STSMO is stabilized when the selected gain satisfies Eq. (45) [23]

$$\begin{cases} r_1 > \frac{\left(4r_2+r_1^2\right)\vartheta}{\left(2r_2+r_1^2\right)} \\ r_2 > \frac{16r_2\vartheta+r_1\vartheta^2}{8r_1} \end{cases} \tag{45}$$

Proof: the Lyapunov function $V_1(x)$ is chosen as:

$$\begin{aligned} V_1(x) &= 2r_2|s_1| + \frac{1}{2}g^2 + \frac{1}{2}\left(r_1|s_1|^{\frac{1}{2}}\operatorname{sgn}(s_1) - g\right)^2 \\ &= \frac{1}{2}\left(4r_2+r_1^2\right)|s_1| + g^2 - r_1 g|s_1|^{\frac{1}{2}}\operatorname{sgn}(s_1) \end{aligned} \tag{46}$$

From Eq. (46):

$$V_1 = \boldsymbol{\sigma}^T\mathbf{Y}\boldsymbol{\sigma} \tag{47}$$

where $r_1 > 0$, $r_2 > 0$; $\boldsymbol{\sigma} = \begin{bmatrix} |s_1|^{\frac{1}{2}}\operatorname{sgn}(s_1) \\ g \end{bmatrix}$; $\mathbf{Y} = \frac{1}{2}\begin{pmatrix} 4r_2+r_1^2 & -r_1 \\ -r_1 & 2 \end{pmatrix}$.

From Eq. (47), taking the derivative of $\boldsymbol{\sigma}$:

$$\begin{aligned} \dot{\boldsymbol{\sigma}} &= \begin{bmatrix} \frac{1}{2}\frac{1}{|s_1|^{\frac{1}{2}}}\cdot\dot{s}_1 \\ \dot{g} \end{bmatrix} \\ &= \frac{1}{|s_1|^{\frac{1}{2}}}\begin{bmatrix} -\frac{1}{2}r_1|s_1|^{\frac{1}{2}}\operatorname{sgn}(s_1) + \frac{1}{2}g + \frac{1}{2}F \\ -r_2|s_1|^{\frac{1}{2}}\operatorname{sgn}(s_1) \end{bmatrix} \\ &= \frac{1}{|s_1|^{\frac{1}{2}}}\left[\begin{bmatrix} -\frac{1}{2}r_1 & \frac{1}{2} \\ -r_2 & 0 \end{bmatrix}\boldsymbol{\sigma} + \begin{bmatrix} \frac{F}{2} \\ 0 \end{bmatrix}\right] \\ &= \frac{1}{|s_1|^{\frac{1}{2}}}(\mathbf{B}\boldsymbol{\sigma} + \boldsymbol{\eta}) \end{aligned} \tag{48}$$

where $\mathbf{B} = \begin{bmatrix} -\frac{1}{2}r_1 & \frac{1}{2} \\ -r_2 & 0 \end{bmatrix}$; $\boldsymbol{\eta}^T = \begin{bmatrix} \frac{F}{2} & 0 \end{bmatrix}$.

Eq. (48) can be reduced as:

$$\dot{\boldsymbol{\sigma}} = \frac{1}{|s_1|^{\frac{1}{2}}}(\mathbf{B}\boldsymbol{\sigma} + \boldsymbol{\eta}) \tag{49}$$

Taking the derivative of $V_1(x)$:

$$\begin{aligned} \dot{V}_1 &= \dot{\boldsymbol{\sigma}}^T\mathbf{Y}\boldsymbol{\sigma} + \boldsymbol{\sigma}^T\mathbf{Y}\dot{\boldsymbol{\zeta}} \\ &= \frac{1}{|s_1|^{\frac{1}{2}}}\begin{bmatrix} \boldsymbol{\sigma}^T\mathbf{B}^T \\ +\boldsymbol{\eta}^T \end{bmatrix}\mathbf{Y}\boldsymbol{\sigma} + \frac{1}{|s_1|^{\frac{1}{2}}}\boldsymbol{\sigma}^T\mathbf{Y}\begin{bmatrix} \mathbf{B}\boldsymbol{\sigma} \\ +\boldsymbol{\eta} \end{bmatrix} \\ &= \frac{1}{|s_1|^{\frac{1}{2}}}\begin{bmatrix} \boldsymbol{\sigma}^T\mathbf{B}^T\mathbf{Y}\boldsymbol{\sigma} \\ +\boldsymbol{\eta}^T\mathbf{Y}\boldsymbol{\sigma} \end{bmatrix} + \frac{1}{|s_1|^{\frac{1}{2}}}\begin{bmatrix} \boldsymbol{\sigma}^T\mathbf{Y}\mathbf{B}\boldsymbol{\sigma} \\ +\boldsymbol{\sigma}^T\mathbf{Y}\boldsymbol{\eta} \end{bmatrix} \\ &= -\frac{1}{|s_1|^{\frac{1}{2}}}\boldsymbol{\sigma}^T\mathbf{X}\boldsymbol{\sigma} + \frac{F}{|s_1|^{\frac{1}{2}}}\mathbf{q}_1^T\boldsymbol{\sigma} \\ &\le -\frac{1}{|s_1|^{\frac{1}{2}}}\boldsymbol{\sigma}^T\mathbf{X}\boldsymbol{\zeta} + \vartheta\mathbf{q}_1^T\boldsymbol{\sigma} \end{aligned} \tag{50}$$

where $F \le \vartheta|s_1|^{\frac{1}{2}}$; $\mathbf{X} = \frac{r_1}{2}\begin{bmatrix} 2r_2+r_1^2 & -r_1 \\ -r_1 & 1 \end{bmatrix}$; $\mathbf{q}_1^T = \left[\left(2r_2+\frac{r_1^2}{2}\right) - \frac{r_1}{2}\right]$.

From Eq. (50), the range of $\vartheta\mathbf{q}_1^T\boldsymbol{\sigma}$ is:

$$\begin{aligned} \vartheta\mathbf{q}_1^T\boldsymbol{\sigma} &= \vartheta\left[\left(2r_2+\frac{r_1^2}{2}\right) - \frac{r_1}{2}\right]\begin{bmatrix} |s_1|^{\frac{1}{2}}\operatorname{sgn}(s_1) \\ g \end{bmatrix} \\ &= \frac{\vartheta}{|s_1|^{\frac{1}{2}}}\begin{bmatrix} \left(2r_2+\frac{r_1^2}{2}\right)|s_1|^{\frac{1}{2}}|s_1|^{\frac{1}{2}}\operatorname{sgn}(s_1) \\ -\frac{r_1}{4}g|s_1|^{\frac{1}{2}} - \frac{r_1}{4}g|s_1|^{\frac{1}{2}} \end{bmatrix} \\ &\le \frac{1}{|s_1|^{\frac{1}{2}}}\left\{\begin{bmatrix} |s_1|^{\frac{1}{2}}\operatorname{sgn}(s_1) & g \end{bmatrix}\begin{bmatrix} \left(4\frac{r_2}{r_1}+r_1\right)\vartheta & -\frac{1}{2} \\ -\frac{1}{2}\vartheta & 0 \end{bmatrix}\begin{bmatrix} |s_1|^{\frac{1}{2}}\operatorname{sgn}(s_1) \\ g \end{bmatrix}\cdot\frac{r_1}{2}\right\} \\ &= \frac{1}{|s_1|^{\frac{1}{2}}}\boldsymbol{\sigma}^T\mathbf{N}\boldsymbol{\sigma} \end{aligned} \tag{51}$$

where $\mathbf{N} = \frac{r_1}{2}\begin{bmatrix} \left(4\frac{r_2}{r_1}+r_1\right)\vartheta & -\frac{1}{2}\vartheta \\ -\frac{1}{2}\vartheta & 0 \end{bmatrix}$.

From Eq. (50) and Eq. (51):

$$\begin{aligned} \dot{V}_1 &\le -\frac{1}{|s_1|^{\frac{1}{2}}}\boldsymbol{\sigma}^T\mathbf{X}\boldsymbol{\sigma} + \delta_1 q_1^T\boldsymbol{\sigma} \\ &\le -\frac{1}{|s_1|^{\frac{1}{2}}}\boldsymbol{\sigma}^T\mathbf{X}\boldsymbol{\sigma} + \frac{1}{|s_1|^{\frac{1}{2}}}\boldsymbol{\sigma}^T\mathbf{N}\boldsymbol{\sigma} \\ &= -\frac{1}{|s_1|^{\frac{1}{2}}}\boldsymbol{\sigma}^T[\mathbf{X}-\mathbf{N}]\boldsymbol{\sigma} \\ &= -\frac{1}{|s_1|^{\frac{1}{2}}}\boldsymbol{\sigma}^T\left[\frac{r_1}{2}\begin{pmatrix} 2r_2+r_1^2-\left(\frac{4r_2}{r_1}+r_1\right)\vartheta & -r_1+\frac{1}{2}\vartheta \\ -r_1+\frac{1}{2}\vartheta & 1 \end{pmatrix}\right]\boldsymbol{\sigma} \\ &= -\frac{1}{|s_1|^{\frac{1}{2}}}\boldsymbol{\sigma}^T[\tilde{\mathbf{X}}]\boldsymbol{\sigma} \end{aligned} \tag{52}$$

Considering the nature of complement of Schur:

$$\begin{cases} 2r_2+r_1^2-\left(\frac{4r_2}{r_1}+r_1\right)\vartheta > 0 \\ 1-\left(-r_1+\frac{1}{2}\vartheta\right)^2\left[2r_2+r_1^2-\left(\frac{4r_2}{r_1}+r_1\right)\vartheta\right]^{-1} > 0 \end{cases} \tag{53}$$

Simplifying Eq. (53), Eq. (54) can be expressed as:

$$\begin{cases} 2r_2r_1+r_1^3-\left(4r_2+r_1^2\right)\vartheta > 0 \\ \left[2r_2+r_1^2-\left(\frac{4r_2}{r_1}+r_1\right)\vartheta\right] > \left(-r_1+\frac{1}{2}\vartheta\right)^2 \end{cases} \tag{54}$$

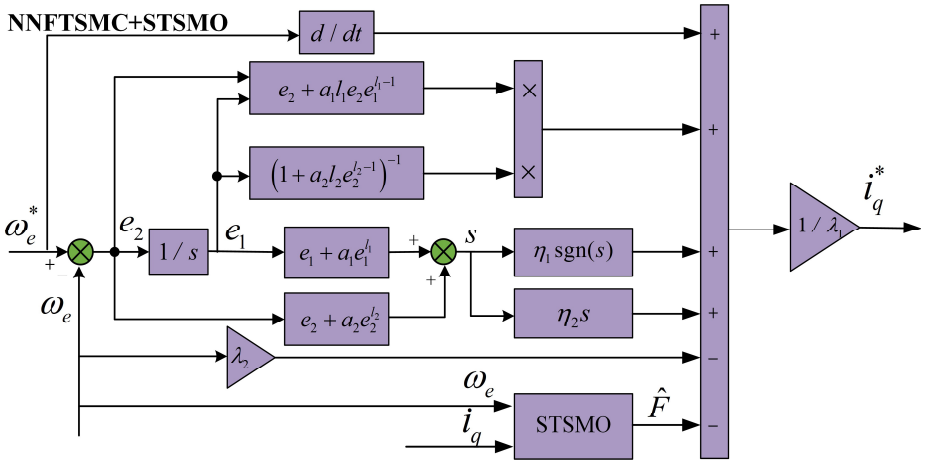

FIGURE 1. The control flowchart of NNFTSMC based on STSMO.

From Eq. (54), the range of values of r_1 and r_2 can be obtained:

$$\begin{cases} r_1 > \frac{\left(4r_2+r_1^2\right)\vartheta}{\left(2r_2+r_1^2\right)} \\ r_2 > \frac{16r_2\vartheta+r_1\vartheta^2}{8r_1} \end{cases} \tag{55}$$

If the range of values of the parameters satisfies Eq. (55), then $\tilde{\mathbf{X}}$ can be made positive definite.

$$\dot{V}_1 \leq -\frac{1}{|s|^{\frac{1}{2}}}\boldsymbol{\sigma}^T\tilde{\mathbf{X}}\boldsymbol{\sigma} \leq -\frac{1}{|s|^{\frac{1}{2}}}\lambda_{\min}\left\{\tilde{\mathbf{X}}\right\}\|\boldsymbol{\sigma}\|_2^2$$

$$\leq -\gamma V_1^{\frac{1}{2}} \leq 0 \tag{56}$$

The STSMO is stabilized from Eq. (56). From Eq. (42)∼Eq. (44), the expression for $\hat{F}$ is expressed as:

$$\hat{F} = G\int_0^t \left[\begin{array}{l} -\lambda_2 x + r_1 |s_1|^{\frac{1}{2}} \mathrm{sgn}(s_1) \\ +\int_0^t r_2 \mathrm{sgn}(s_1)\, dt \end{array}\right] dt \tag{57}$$

Substituting Eq. (57) into Eq. (22), i_q^* is expressed as:

$$i_q^* = \frac{1}{\lambda_1}\left[\begin{array}{l} \left(1 + a_2 l_2 e_2^{l_2-1}\right)^{-1} \cdot \left(e_2 + a_1 l_1 e_2 e_1^{l_1-1}\right) \\ +\dot{\omega}_e^* - \lambda_2\omega_e + \eta_1 \mathrm{sgn}(s) + \eta_2 s - \hat{F} \end{array}\right] \tag{58}$$

The saturation function $H(s)$ is designed as [24]:

$$H(s) = \frac{s}{|s| + \varepsilon} \tag{59}$$

where $\varepsilon > 0$. Figure 1 shows the control flowchart of NNFTSMC based on STSMO. Figure 2 shows the structure of STSMO.

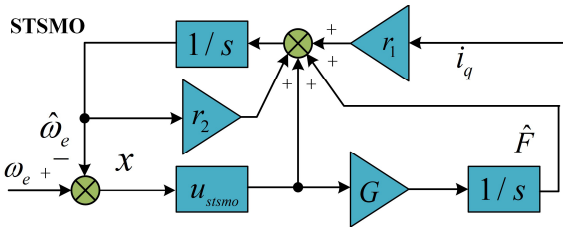

FIGURE 2. The structure of STSMO.

4. ANALYSIS OF SIMULATION

Comparing the NNFTSMC algorithm based on STSMO with PI and SMC+SMO in the MATLAB/Simulink platform, Table 1 shows the parameters of PMSM, and Table 2 shows the control parameters of PI/SMC+SMO/NNFTSMC+STSMO. Figure 3

TABLE 1. The parameters of PMSM.

Parameters	Units	Values
Dc voltage/u_{dc}	V	600
Stator resistance/R_s	Ω	2.75
Rated speed/n_N	r/min	1900
Pole number/n_p	pairs	2
q-axis inductance/L_q	H	0.009
d-axis inductance/L_d	H	0.004
Inertia/J	kg·m^2	0.029
Coefficient of viscous friction/B	N·m·s/rad	0.001
Magnetic flux/ψ_f	Wb	0.12

TABLE 2. The control parameters of PI/SMC+SMO/NNFTSMC +STSMO.

PI	SMC+SMO	NFTSMC+STSMO
$K_p = 100$	$C_1 = 105$	$a_1 = 0.006$
$K_I = 1000$	$k_1 = 0.52$	$a_2 = 0.03$
/	$k_2 = 0.0051$	$l_1 = 7/5$
/	$k_3 = 1050$	$l_2 = 5/3$
/	$\lambda_1 = 20$	$\eta_1 = 0.1$
/	/	$\eta_2 = 0.01$
/	/	$r_1 = 5000$
/	/	$r_2 = 0.5$

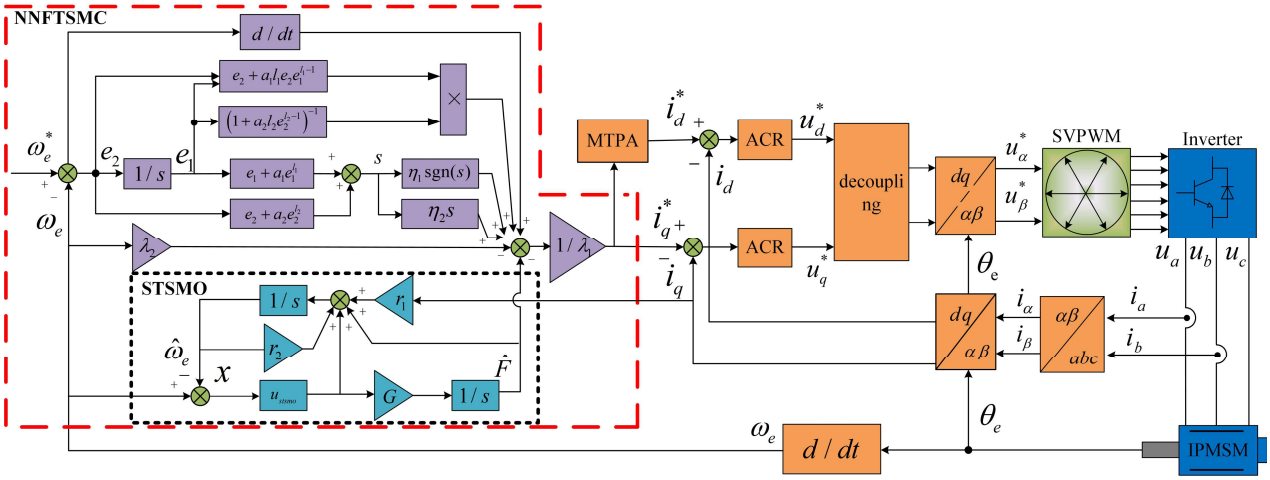

FIGURE 3. The general block diagram of the control of the PMSM drive system.

shows the general block diagram of the control of the PMSM drive system.

Remark 1: The values of λ_1 and λ_2 in the algorithm of this paper are rounded by $\lambda_1 = 3n_p^2\psi_{ext}/2J$ and $\lambda_2 = -B/J$. In the SMC+SMO algorithm, the sliding mode surface is $s = c_1e_1 + e_2$; the exponential convergence law is $\dot{s} = -k_1\text{sgn}(s) - k_2s$; and the SMO is designed to estimate the total system perturbation in real time and to feedback the SMC. The experimental working condition of the setup PMSM is shown in Table 3.

TABLE 3. The experimental condition of PI/SMC+SMO/NNFTSMC +STSMO.

time/s	magnitude of change	Scope of change
1.0	R_s/Ω	$2 \rightarrow 2.6$
1.5	ψ_f/Wb	$0.12 \rightarrow 0.09$
2.0	n^*/r/min	$1000 \rightarrow 2000$
2.5	L_d/H	$0.004 \rightarrow 0.0031$
3.0	L_q/H	$0.009 \rightarrow 0.0061$
3.5	B/N·m·s/rad	$0.001 \rightarrow 0.0041$
4.0	J/kg·m^2	$0.029 \rightarrow 0.041$
4.5	T_L/N·m	$15 \rightarrow 20$

Figure 4 shows the simulation comparison of PI/SMC+SMO/NNFTSMC+STSMO. Figure 4(a) shows the comparison of speed for PI/NNFTSMC+STSMO. Figure 4(b) shows the comparison of speed for SMC+SMO/NNFTSMC+STSMO. From Figure 4(a) and Figure 4(b), in the speed regulation condition 0 r/min–1000 r/min–2000 r/min, there is a large overshoot of the PI, which takes some time to recover. The SMC+SMO does not have a large overshoot compared with PI, but it has a longer time to converge to a given speed compared with NNFTSMC+STSMO. Overall, the average convergence time of rotational speed of PI is 0.35 s, while the average convergence time of rotational speed of SMC+SMO is 0.2 s due to its nonlinear characteristics, which makes the control better than PI; NNFTSMC+STSMO adopts a new NFTSM surface, which solves the problem of slow convergence of the traditional ISM surface in SMC+SMO, and the average convergence time of the rotational speed is 0.15 s, with the optimal overall control effect.

Figure 4(c) shows the comparison of torque for PI/NNFTSMC+STSMO, 4(d) shows the comparison of torque for SMC+SMO/NNFTSMC+STSMO. From Figure 4(c) and Figure 4(d) when the internal electromagnetic parameters (R_s, L_d, L_q, ψ_f) and mechanical parameters $(J,\ B)$ of the PMSM are subject to nonlinear time-varying regression, the overall PMSM system controlled by PI/SMC+SMO/NNFTSMC+STSMO is affected to some extent but the torque of the PMSM driven by NNFTSMC+STSMO is the most stable, and the torque pulsation is the smallest. With the PMSM controlled by PI and SMC+SMO in the nonlinear change of J and B, the output torque pulsation of the PMSM drive system becomes larger, which generates pulsating harmonics to a certain extent, and it is not conducive to the stable operation of the PMSM drive system. With the PMSM controlled by PI and SMC+SMO in the nonlinear change of R_s, L_d, L_q, and ψ_f, the output torque of PMSM drive system has a large overshoot at the moment of change, and the transient steady state control accuracy of NNFTSMC+STSMO is optimal.

Figure 4(e) shows the comparison of d-axis current for PI /NNFTSMC+STSMO, and Figure 4(f) shows the comparison of d-axis current for SMC+SMO/NNFTSMC+STSMO. Figure 4(g) shows the comparison of q-axis current for PI/NNFTSMC+STSMO, and Figure 4(h) shows the comparison of q-axis current for SMC+SMO/NNFTSMC+STSMO.

From Figure 4(e)∼Figure 4(h), the d-q axis currents controlled by PI and SMC+SMO have some overshoot in the system transient state and large pulsations in the system steady state. In contrast, the d-q axis currents pulsation response of the NNFTSMC+STSMO is fast enough to reach the reference value quickly, and the steady state pulsation is small. This is mainly attributed to the fact that the STSMO in NNFTSMC+ STSMO can accurately estimate the total system disturbance

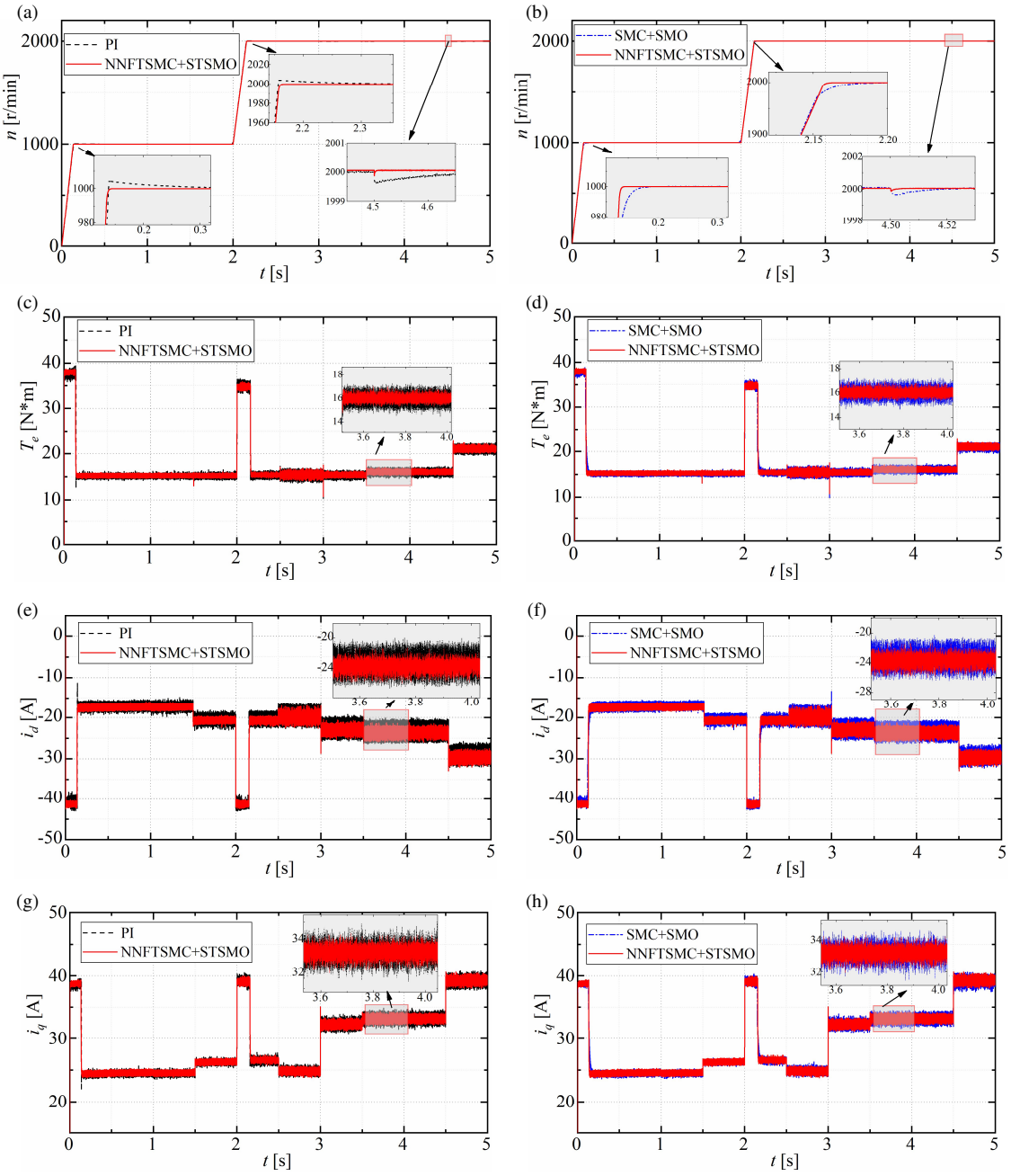

FIGURE 4. Simulation comparison of PI/SMC+SMO/NNFTSMC+STSMO. (a) Comparison of speed for PI/NNFTSMC+STSMO. (b) Comparison of speed for SMC+SMO/NNFTSMC+STSMO. (c) Comparison of torque for PI/NNFTSMC+STSMO. (d) Comparison of torque for SMC+SMO/NNFTSMC+STSMO. (e) Comparison of d-axis current for PI/NNFTSMC+STSMO. (f) Comparison of d-axis current for SMC+SMO/NNFTSMC+STSMO. (g) Comparison of q-axis current for PI/NNFTSMC+STSMO. (h) Comparison of q-axis current for SMC+SMO/NNFTSMC+STSMO.

F and feed back to NNFTSMC. Figure 5 shows the simulation comparison of the SMO/STSMO. From Figure 5(a), SMO has poor performance in tracking the rotational speed of system, and the rotational speed tracking error does not converge to 0; while STSMO can track the rotational speed of system quickly, and the rotational speed tracking error converges to 0 stably. From Figure 5(b), both SMO and STSMO can effectively estimate the F of the system, but when the electromagnetic and mechanical parameters of the PMSM are changed, there is some jitter in the total disturbance of the system observed by SMO, and the overall observational performance is poor, which is mainly due to the large gain of the k_3 in SMO. If k_3 is used with small gain, SMO cannot accurately track the rotational speed of system, and it cannot accurately observe the F. The STSMO can effectively solve this problem by accurately tracking the speed of system while better observing the F of the system.

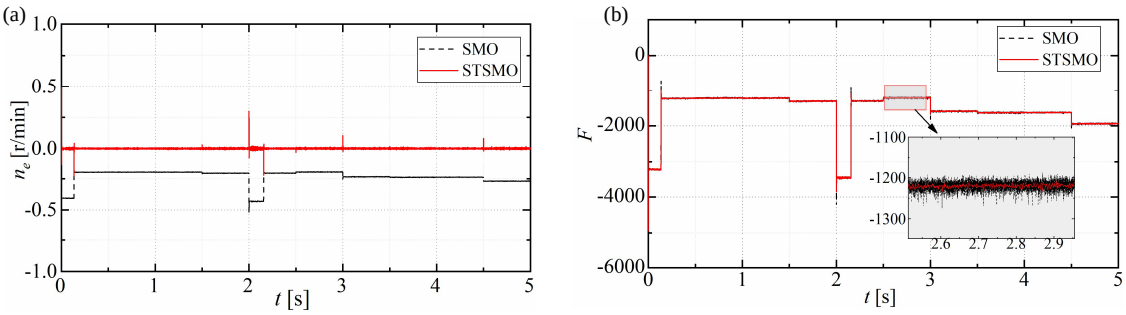

FIGURE 5. Simulation comparison of SMO/STSMO. (a) The tracking error of rotational speed. (b) The unknown part of the total perturbation F.

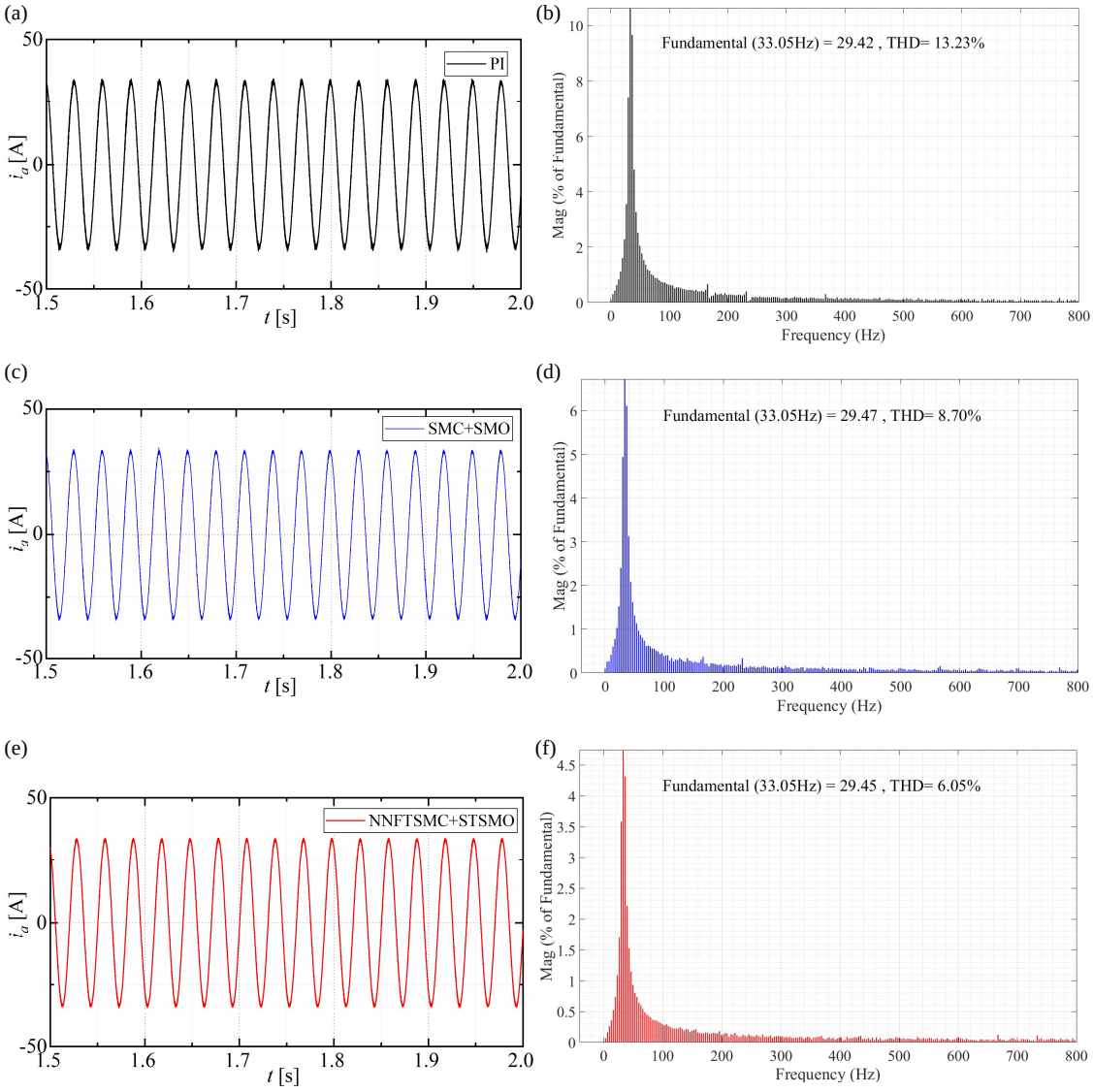

FIGURE 6. The THD analysis for PI/SMC+SMO/NNFTSMC+STSMO. (a) A-phase current of PI. (b) The THD value of PI. (c) A-phase current of SMC+SMO. (d) The THD value of SMC+SMO. (e) A-phase current of NNFTSMC+STSMO. (f) The THD value of NNFTSMC+STSMO.

Figure 6 shows the Total Harmonic Distortion (THD) analysis for PI/SMC+SMO/NNFTSMC+STSMO under 1.5 s–2.0 s steady state operation conditions. From Figure 6(a)∼Figure 6(f), the total waveform of i_a for PI has more harmonic components with THD value of 13.23%. The SMC+SMO uses the SMO to observe the F of the system and feeds back to the SMC, which effectively reduces the harmonic components in the total waveform of i_a, and the value of THD is reduced to 8.70%. Compared with PI and SMC+SMO, NNFTSMC+STSMO has lower total waveform

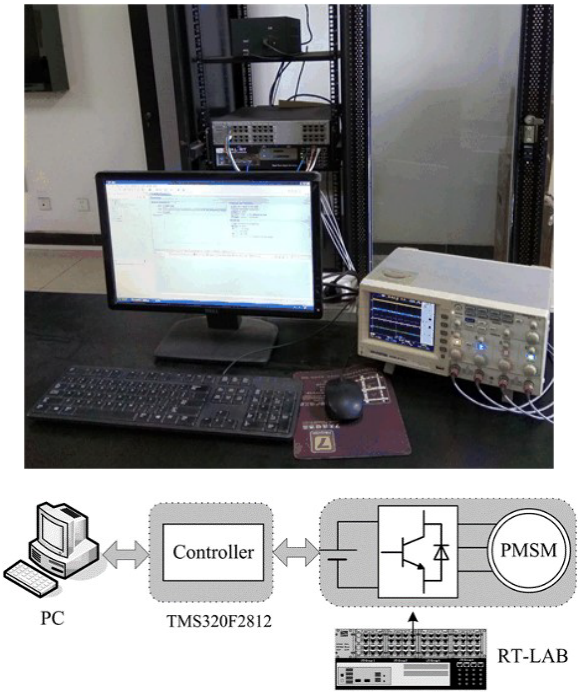

FIGURE 7. The experimental platform of RT-LAB.

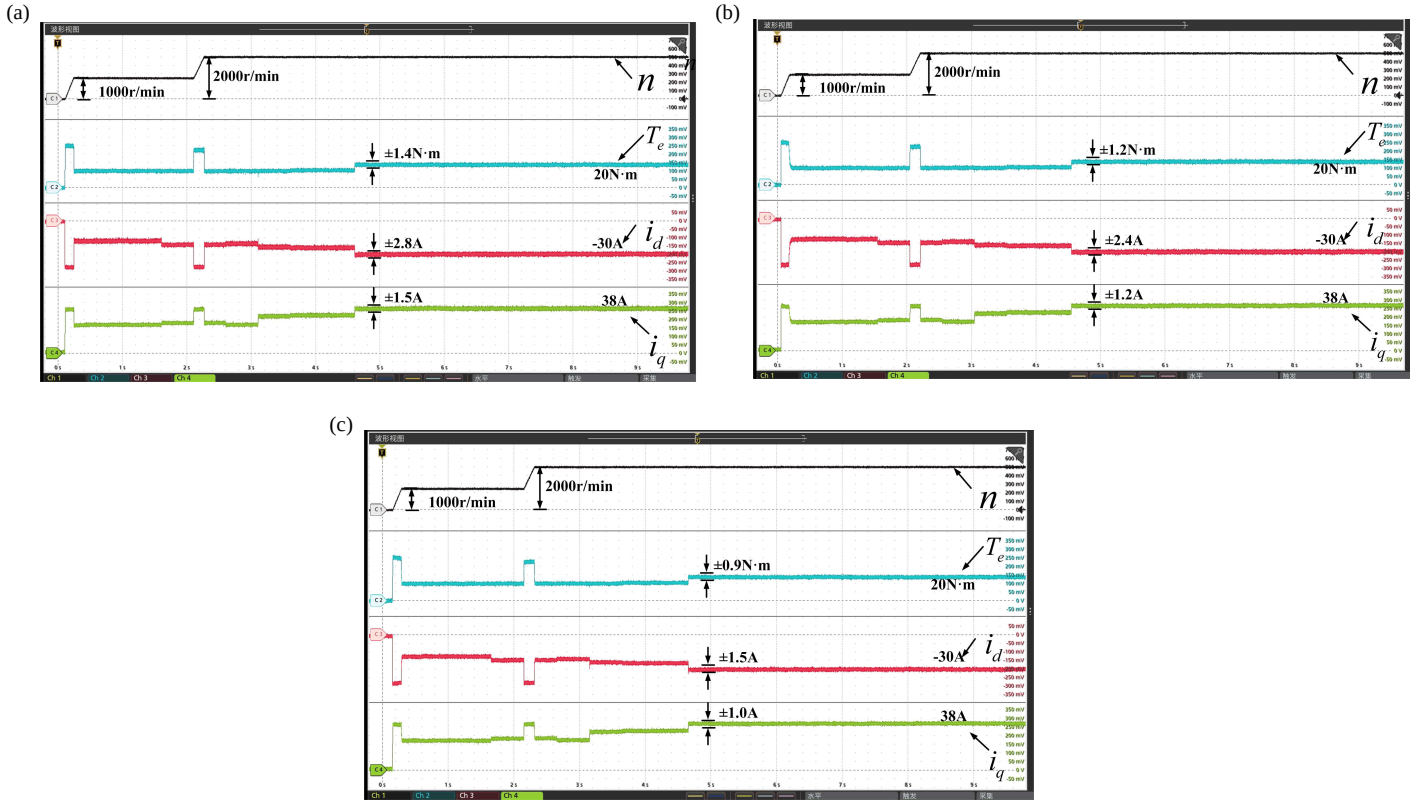

FIGURE 8. The RT-LAB experimental comparison of PI/SMC+SMO/NNFTSMC+STSMO. (a) PI. (b) SMC+SMO. (c) NNFTSMC+STSMO.

THD value of 6.05%, which is is mainly attributed to the fact that NNFTSMC is paired with the more accurate observer, which further reduces the harmonic content, effectively suppresses the current pulsation, and improves the quality of the currents in the PMSM drive system.

TABLE 4. The performance comparison of PI/SMC+SMO/NNFTSMC+STSMO.

Performance indicators	PI	SMC+SMO	NNFTSMC+STSMO
torque pulsation	14.11%	10.16%	7.56%
i_a THD	13.23%	8.70%	6.05%
static differential of speed	0.1/0.2	0.05/0.1	0.02/0.03
Response time of speed	0.35/0.35	0.2/0.2	0.14/0.16

5. ANALYSIS OF RT-LAB SEMI-PHYSICAL EXPERIMENTS

Figure 7 shows the semi-physical experimental platform of RT-LAB [25]. In Figure 7, the PMSM drive system is simulated by RT-LAB [26]. Figure 8 shows the RT-LAB experimental comparison of PI/SMC+SMO/NNFTSMC+STSMO, and the simulation parameters are consistent with the experimental ones.

From Figure 7, RT-LAB (OP5600) uses a real DSP controller of model TMS320F2812 for simulate the rest of the components of the PMSM system, such as the PMSM and the inverter. The HILP system used in this paper adopts the structure of real controller + virtual controlled object to model the controlled object of the system, and the real-time simulator runs the solved model to interact with the real controller. Through the HILP semi-physical simulation platform experiment, experimental results consistent with the actual motor can be obtained. The implementation of the control algorithm is mainly to modify the algorithm in the Simulink environment, and then download it into the RT-Lab controller to ensure that the platform parameters and indicators are normal and start running. Comparing the simulation results in Figure 4 with the experimental results in Figure 8, it can be seen that the overall performance of the drive system controlled by PI is limited. Compared with the PI, the performance of the drive system with SMC+SMO is increased, but the speed convergence is slower, and the transient overshoot is still present in the output torque and d-q axis currents. The PMSM drive system of NNFTSMC+STSMO can effectively improve the shortcomings of PI and SMC+SMO to achieve the requirement of high precision control. Table 4 shows the performance comparison of PI/SMC+SMO/NNFTSMC+STSMO.

6. CONCLUSION

Aiming at the problem that the speedloop PI and SMC+SMO controllers cannot realize the fast convergence of the system when the PMSM undergoes parameters ingress, this paper designs an algorithm of NNFTSMC base on STESMO for PMSM. This method proposes a new NFTSM surface to design the PMSM speedloop controller. Then, it proposes a super-twisting control law to design STESMO to observe the total system perturbation in real time and performs perturbation compensation to NNFTSMC. By comparing the simulation and RT-Lab semi-physical experiments, it is verified that the proposed algorithm can effectively suppress the system jitter and weaken the steady state pulsation while preventing the transient overshoot during the parameters ingress and load mutation of PMSM.

ACKNOWLEDGEMENT

This work was supported by the Natural Science Foundation of China (NSFC) under Grant 61473117, Grant 62173137, and Grant 2021YFF0501100, and in part by Postgraduate Scientific Research Innovation Project of Hunan Province under Grant CX20231107.

REFERENCES

[1] Shi, P., "A review of position sensorless compound control for PMSM drives," *World Electric Vehicle Journal*, Vol. 14, No. 2, 34, 2023.

[2] Wang, F., Y. Wei, H. Young, *et al.*, "Continuous-control-set model-free predictive fundamental current control for PMSM system," *IEEE Transactions on Power Electronics*, Vol. 38, No. 5, 5928–5938, 2023.

[3] Bangi, M. S. F. and J. S.-I. Kwon, "Deep hybrid model-based predictive control with guarantees on domain of applicability," *AIChE Journal*, Vol. 69, No. 5, e18012, 2023.

[4] Ye, Z., D. Zhang, C. Deng, H. Yan, and G. Feng, "Finite-time resilient sliding mode control of nonlinear UMV systems subject to DoS attacks," *Automatica*, Vol. 156, 111170, 2023.

[5] Badings, T., L. Romao, A. Abate, *et al.*, "Robust control for dynamical systems with non-Gaussian noise via formal abstractions," *Journal of Artificial Intelligence Research*, Vol. 76, 341–391, 2023.

[6] Mohd Zaihidee, F., S. Mekhilef, and M. Mubin, "Robust speed control of PMSM using sliding mode control (SMC) — A review," *Energies*, Vol. 12, No. 9, 1669, 2019.

[7] Niu, S., W.-H. Chen, X. Lu, and W. Xu, "Integral sliding mode control design for uncertain impulsive systems with delayed impulses," *Journal of The Franklin Institute*, Vol. 360, No. 17, 13 537–13 573, 2023.

[8] Xu, Y., S. Li, and J. Zou, "Integral sliding mode control based deadbeat predictive current control for PMSM drives with disturbance rejection," *IEEE Transactions on Power Electronics*, Vol. 37, No. 3, 2845–2856, 2021.

[9] Zhao, K., W. Liu, R. Zhou, W. Dai, S. Wu, P. Qiu, Y. Yin, N. Jia, J. Yi, and G. Huang, "Model-free fast integral terminal sliding-mode control method based on improved fast terminal sliding-mode observer for PMSM with unknown disturbances," *ISA Transactions*, Vol. 143, 572–581, 2023.

[10] Li, X., J. Liu, K. Zhao, Y. Yin, and L. Zou, "Improved non-singular fast terminal sensor-less sliding mode control of IPMSM considering external disturbance and parameter perturbation," *Progress In Electromagnetics Research B*, Vol. 102, 81–98, 2023.

[11] Zhao, K., W. Liu, T. Yin, R. Zhou, W. Dai, and G. Huang, "Model-free sliding mode control for PMSM drive system based on ultra-local model," *Energy Engineering: Journal of The As-*

sociation of Energy Engineering, Vol. 119, 767–780, 2022.

[12] Zhao, K., J. Yi, W. Liu, *et al.*, "A model-free super-twisting fast terminal sliding mode control method for PMSM," *Power System Protection and Control*, Vol. 51, No. 22, 88–98, 2023.

[13] Yu, T., W. Yi, Z.-H. Wu, *et al.*, "Decoupled nonsingular fast terminal sliding mode control based on super twisted algorithm," *Control Engineering of China*, Vol. 27, No. 2, 271, 2020.

[14] Li, X., J. Liu, Y. Yin, and K. Zhao, "Improved super-twisting non-singular fast terminal sliding mode control of interior permanent magnet synchronous motor considering time-varying disturbance of the system," *IEEE Access*, Vol. 11, 17 485–17 496, 2023.

[15] Wen, D., X. Zhu, Z. Cheng, Y. Zhang, and W. Zhang, "Sensorless control of interior permanent magnet synchronous motor with triangular transform current self-demodulation in the estimating d-q axis," *Progress In Electromagnetics Research B*, Vol. 103, 75–99, 2023.

[16] Xiao, Q., Z. Yu, W. Zhang, Z. Tang, and Z. Cheng, "Hybrid-vector model predictive flux control for PMSM considering narrow pulse," *Progress In Electromagnetics Research C*, Vol. 137, 235–249, 2023.

[17] Yi, Z., X. Li, Y. Yin, J. Liu, and K. Zhao, "Deep flux weakening control of IPMSM based on d-axis current error integral regulator," *Progress In Electromagnetics Research M*, Vol. 118, 163–175, 2023.

[18] Xiao, Q., Z. Tang, W. Zhang, Z. Yu, and Z. Cheng, "A robust model predictive current control strategy with low complexity for PMSM," *Progress In Electromagnetics Research C*, Vol. 136, 161–174, 2023.

[19] Yang, Y., M. Deng, S. Li, and Y. Zhang, "Based on fast non-singular terminal sliding of PMSM model-free control," *Progress In Electromagnetics Research C*, Vol. 137, 139–153, 2023.

[20] Yang, Y., "Research on high-order sliding mode-weak magnet optimization composite control of PMSM," Ph.D. dissertation, Hunan University of Technology, Zhuzhou, Hunan, China, 2023.

[21] Yu, Y. and X. Liu, "Model-free fractional-order sliding mode control of electric drive system based on nonlinear disturbance observer," *Fractal and Fractional*, Vol. 6, No. 10, 603, 2022.

[22] Yue, Y., Y. Geng, and W. Wang, "Continuous nonsingular fast terminal sliding mode control for speed tracking of PMSM based on finite time disturbance observer," *Processes*, Vol. 10, No. 7, 1407, 2022.

[23] Li, X., J. Liu, K. Zhao, Y. Yin, and L. Zou, "An improved model-free sliding mode control algorithm of super-twisting for SPMSM," *Progress In Electromagnetics Research C*, Vol. 135, 195–210, 2023.

[24] Fu, D., X. Zhao, and J. Zhu, "A novel robust super-twisting nonsingular terminal sliding mode controller for permanent magnet linear synchronous motors," *IEEE Transactions on Power Electronics*, Vol. 37, No. 3, 2936–2945, 2021.

[25] Wen, D., W. Zhang, Z. Li, Z. Tang, Y. Zhang, and Y. Ling, "Dual cost function model predictive control for PMSM," *Progress In Electromagnetics Research C*, Vol. 131, 171–184, 2023.

[26] Xiao, Q., Z. Liu, Y. Zhang, Z. Li, B. Luo, and T. Wang, "Improved higher-order sliding mode controller for model predictive current control of PMSM," *Progress In Electromagnetics Research C*, Vol. 123, 117–133, 2022.